

Supplemental Information (SI)

Zn²⁺-blocking effects of proton-rich polyaniline layer enable Ah-level Zn-MnO₂ battery

Qi Li,^{‡a} Meng Xu,^{‡a} Shiqiang Wei,^b Anuj Kumar,^c Kovan Khasraw Abdalla,^a Yueyang Wang,^a
Linfeng Yu,^a Mengyao Liu,^a Xiangrong Jin,^a Jiazhan Li,^a Li Song,^b Yi Zhao^{*a} and Xiaoming Sun^{*a}

^aState Key Laboratory of Chemical Engineering, College of Chemistry,
Beijing University of Chemical Technology, Beijing 100029, PR China

E-mail: sunxm@mail.buct.edu.cn; zybattery@buct.edu.cn

^bCAS Center for Excellence in Nanoscience, University of Science and Technology of China,
Hefei 230029, China Advanced Technology Research Institute

^cDepartment of Chemistry, GLA University, Mathura, UP-281406, India

[‡]These authors contributed equally to this work.

Section S1. Experimental section

1.1 Material Synthesis

Synthesis of P-MnO₂ and MnO₂ cathode: The polyaniline (PANI) modified α -MnO₂ cathode (denoted as P-MnO₂) was synthesized by the microenvironment modulating of MnO₂ through the mechanical stirring method. Firstly, nano manganese dioxide powder (MnO₂) and PANI were employed as active substances to prepare the P-MnO₂ cathode materials. During preparation process, MnO₂ and PANI was mixed in DI water for 24 hours at 60 °C. Then the resulting black precipitates were centrifuged, washed with DI water for several times, and dried in a vacuum at 60 °C for 12 h. Finally, the obtained powder, carbon nanotubes (CNTs) and polyvinylidene fluoride (PVDF) were homogeneously mixed in NMP at a mass ratio of 7:2:1 to prepare the P-MnO₂ slurry *via* the mechanical grinding approach (**Scheme 1**). Before coating, the carbon cloth (CC) was cut into an area of 2×3 cm² and treated with concentrated nitric acid to form a hydrophilic surface (**Figure S1a**). Then, the P-MnO₂ sample based on CC was fabricated through the blade coating machine after dried at 60 °C for 24 h (**Figures S1b, c**). Thereinto, the active loading of P-MnO₂ could be controlled within 2.0 mg cm⁻² by adjusting the coating thickness. The contrastive sample, manganese dioxide cathode (designated as MnO₂), was fabricated without the addition of PANI.

1.2 Material Characterizations

The morphology and elemental composition analysis of P-MnO₂, MnO₂ and PANI were obtained by field-emission scanning electron microscopy (FE-SEM) with energy dispersion spectrum (EDS) mapping equipment (Hitachi Regulus 8230, 10.0 kV) and high-resolution

transmission electron microscopy (HRTEM, JEOL JEM-F200) with EDS. X-ray diffraction data (XRD) were collected from D8 ADVANCE Davinci Bruker equipped with Cu-K α radiation. The valence states of surface chemical elements and the internal molecular structure were respectively operated on X-ray photoelectron spectroscopy (XPS, ESCALAB 250 Thermo Fisher Scientific), Raman spectrometer with Ar laser excitation source at 532 nm (LabRAM Aramis, HORIBA Jobin Yvon) and Fourier transform infrared spectrometer (FTIR, Nicolet 6700, Thermo Fisher Scientific). The chemical coordination environment of Mn in P-MnO₂ and MnO₂ was characterized by X-ray absorption spectroscopy (XAS). The K-edge XAS spectra of Mn were acquired at the 1W1B station of the Beijing Institute of High Energy Physics. The Scotch[®]Magic[™] tape was covered with the powder sample to collect XAS spectral data on the K-edge of Mn in fluorescence mode, with the energy regulated by a silicon (111) monochromator. Moreover, the transmission mode was employed for Mn foil, MnO, MnO₂, Mn₂O₃, Mn₃O₄ and MnPc. The aberration-corrected high-angle annular dark-field scanning transmission electron microscope (HAADF-STEM, JEOL JEM-ARM200F, country), is equipped with a spherical aberration corrector at 200 kV. The Specific surface area and pore-size distribution of P-MnO₂ and MnO₂ were performed on a Micromeritics ASAP 2020 adsorption analyzer based on the Brunner-Emmet-Teller (BET) measurements. The content of elements in the solution was measured by inductively coupled plasma optical emission spectrometry (ICP/OES, Agilent 725ES). And the surface composition of the P-MnO₂ cathode was studied by time of flight secondary ion mass spectrometry (TOF-SIMS, TOF-SIMS 5 iontof). To better investigate the chemical reactions of the P-MnO₂ cathode, *ex-situ* tests of XRD, SEM-EDS, XPS and ICP/OES were carried out at specific voltage values during charging/discharging process.

1.3 Electrochemical Measurements

The CR2032-type coin cells were assembled in air by using P-MnO₂ and MnO₂ as cathodes, a glass Fiber membrane soaked with 2 M ZnSO₄ and 0.2 M MnSO₄ solution as the separator, and a 70- μ m thick polished Zn foil (99.9% trace metal basis) as the counter electrode. The high-loading

P-MnO₂ cathode materials and assembled Ah-level pouch cells are successfully achieved through optimized slurry preparation and electrode fabrication processes. Specifically, P-MnO₂, and carbon nanotubes were first mixed in deionized water at a mass ratio of 7:2, followed by high-rate mixing at 2000 rpm for 30 minutes to form a homogeneous slurry. After the resulted precipitate was collected by filtration and then washed with DI water and absolute ethanol repeatedly. Then, 10 wt% PTFE binder was added into the obtained PANI/carbon nanotubes mixture at low speed to obtain a dough-like material with excellent extensibility. The material was then repeatedly calendered (10 passes at 0.55 mm gap) using a dual-roller machine at 60 °C to achieve complete fiberization. The resulting P-MnO₂ was cut into 7.6 × 9 cm sheets and laminated onto both sides of a 100-mesh stainless steel current collector under appropriate pressure. After vacuum drying at 80 °C for 12 hours, high-quality electrodes with an areal density of 23.5 mg cm⁻² were obtained. The Ah-level Zn//P-MnO₂ pouch cell was assembled with three P-MnO₂ cathodes and stacked alternately four 60 μm zinc foil anodes (33 mg cm⁻²), was impregnated with 2 M ZnSO₄ + 0.2 M MnSO₄ electrolyte before being vacuum-sealed in aluminum laminate packaging. Finally, the pouch cell was tested electrochemical performance under 30 mA and 50 mA, respectively. Cyclic voltammetry (CV) and electrochemical impedance spectroscopy (EIS) profiles were tested on a CorrTest CS2350H electrochemical workstation (Wuhan CorrTest Instrument Corp., Ltd. China), with a frequency range from 10,000 Hz to 0.01 Hz at 10 mV. The galvanostatic charge–discharge (GCD) experiments of the full zinc ion batteries were carried out using a NEWARE Battery Test System (Neware, Shenzhen, China) at room temperature. In-situ pH test was performed in a pH meter (PHBJ-260).

Section S2. Calculation Methods

2.1 Calculation Details

All DFT calculations were performed using the Vienna Ab-initio Simulation Package (VASP).¹⁻

²⁾ The exchange-correlation effects were described by the Perdew-Burke-Ernzerhof (PBE)

functional within the generalized gradient approximation (GGA) method.^[3-4] Core-valence interactions were accounted for using the projected augmented wave (PAW) method.^[5] A plane wave energy cutoff of 400 eV was employed for expansions. Structural optimization was carried out with energy and force convergence criteria set at 1.0×10^{-4} eV and 0.05 eV \AA^{-1} , respectively. The Brillouin zone was sampled with the $3 \times 3 \times 1$ K-point grid. Grimme's DFT-D3 methodology was utilized to describe dispersion interactions.^[6]

The dissolution energy (E_{dis}) of Mn is determined by calculation:

$$E_{\text{dis}} = E_{\text{MnO}_2\text{-Mnv}} + E_{\text{Mn}} - E_{\text{MnO}_2}$$

where $E_{\text{MnO}_2\text{-Mnv}}$ and E_{Mn} represent the total energies of $\text{MnO}_2\text{-Mnv}$ and pure MnO_2 systems, respectively. E_{Mn} represents the energy of a single atom of Mn in the bulk phase.

The adsorption energies (E_{ads}) of H and Zn are calculated as follows

$$E_{\text{ads}} = E_{*H} - E_H - E_{\text{Sub}} \qquad E_{\text{ads}} = E_{*Zn} - E_{Zn} - E_{\text{Sub}}$$

The insertion energies (ΔE) of H and Zn are calculated as follows

$$\Delta E = E_{\text{sub-H}} - E_H - E_{\text{Sub}} \qquad \Delta E = E_{\text{sub-Zn}} - E_{Zn} - E_{\text{Sub}}$$

where E_H and E_{*H} represent the energies before and after the adsorption of H on the substrates, respectively. Similarly, E_{Zn} and E_{*Zn} represent the energies before and after the adsorption of Zn on the substrates. In addition, $E_{\text{sub-H}}$ and $E_{\text{sub-Zn}}$ represent the energies after the insertion of H and Zn on the substrates, respectively. The term E_{sub} denotes the energy of MnO_2 and P- MnO_2 surfaces.

2.2 Ion Diffusion Coefficient

Calculation of Ion Diffusion Coefficient (D) from EIS Tests: Based on the low-frequency spectrum of EIS, the ion diffusion coefficient can be calculated by the following equation:

$$Z' = R_s + R_f + R_{ct} + \sigma_w \omega^{-0.5} \quad (1)$$

$$D = R^2 T^2 / 2 A^2 n^4 F^4 C^2 \sigma_w^2 \quad (2)$$

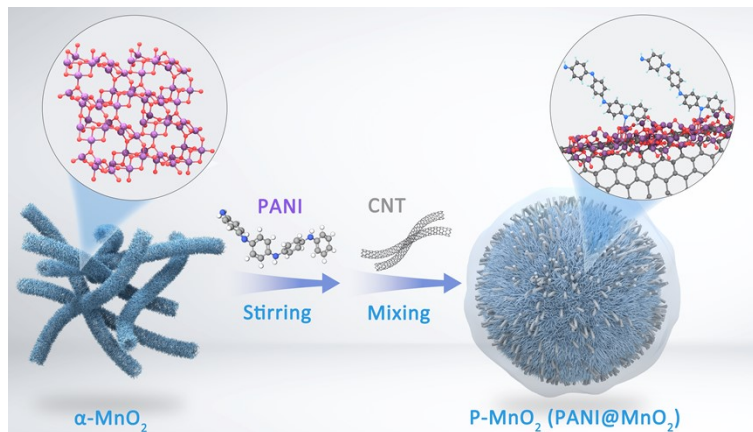
Where ω , A, n, F, C, R and T represent the angular frequency, electrode area, number of electrons involved in each chemical reaction, Faraday's constant (96500 C mol⁻¹), ionic molar concentration, gas constant (8.314 J mol⁻¹·K⁻¹) and test temperature (298 K) respectively. The fundamental part Z' comprises of the bulk resistance (R_s), charge-transfer resistance (R_{ct}), and resistance to mass transfer, and the values of R_s and R_{ct} are obtained by fitting the equivalent circuit.

Calculation of Ion Diffusion Coefficient (D): After the assembled battery is allowed to stand, it is discharged/charged at 0.2 A g⁻¹ for 10 cycles, followed by the galvanostatic intermittent titration technique (GITT) measurement to ensure that the test is in a stable state. Subsequently, the battery is discharged or charged at 0.2 A g⁻¹ for 4 minutes followed by 8 minutes to reach voltage equilibrium. This procedure is repeatedly applied during the charging/discharging process of the battery. Based on the relationship between potential and time, D can be calculated using the following equation: $\Delta E_s / \Delta E_t$ represents a linear relationship with time.

$$D = \frac{4}{\pi \tau} \left(\frac{n_m V_m}{S} \right)^2 \left(\frac{\Delta E_s}{\Delta E_t} \right)^2 \quad (3)$$

where τ is the constant current pulse time, n_m is the number of moles, V_m is the molar volume, S is the electrode/electrolyte contact area, ΔE_s is the total change of the voltage caused by pulses and ΔE_t is the voltage change during constant current charging/discharging.

Section S3. Supplementary Characterizations



Scheme 1 Schematic preparation of P- MnO_2 through mechanical stirring method.

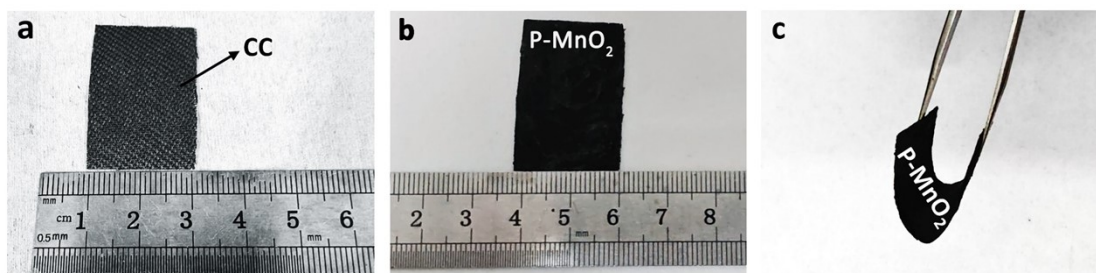


Fig. S1 The optical images of (a) carbon cloth, (b, c) P- MnO_2 sample.

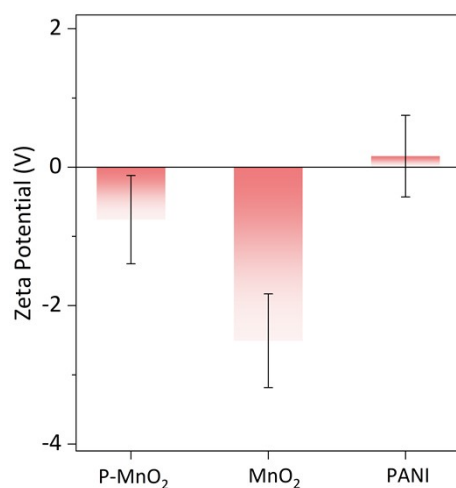


Fig. S2 Zeta potential of P-MnO₂, MnO₂ and PANI.

In a dispersion medium of 2 M ZnSO₄ + 0.2 M MnSO₄, the Zeta potential of PANI is around 0.16 V, while that of MnO₂ is around -2.51 V. The opposite signs of both values indicate a significant electrostatic complementarity in interfacial electric double layers. After mechanical stirring treatment, HRTEM image (**Fig. 1c**) reveals that the self-driven assembly between PANI and MnO₂ particles occurs due to electrostatic attraction, resulting in the formation of a heterostructure that enhances the structural stability of P-MnO₂. Furthermore, at the interface between these two phases, there exist electrostatic coordination interactions based on -NH⁺ (PANI) and -O⁻/Mn-O⁻ (MnO₂), which facilitate the formation of Mn-N bonds.

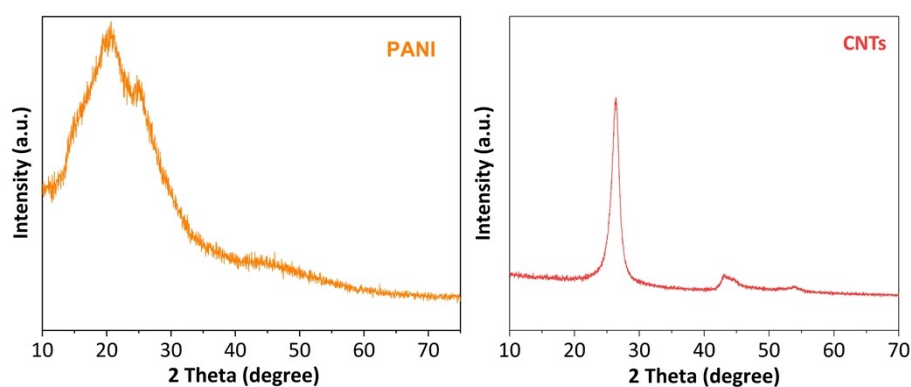


Fig. S3 XRD profiles of PANI and CNTs powders, respectively.

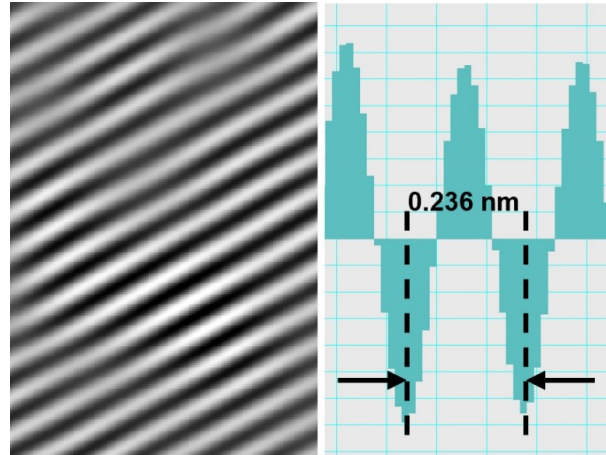


Fig. S4 FFT pattern (left) and normalized intensity variations (right) of P-MnO₂.

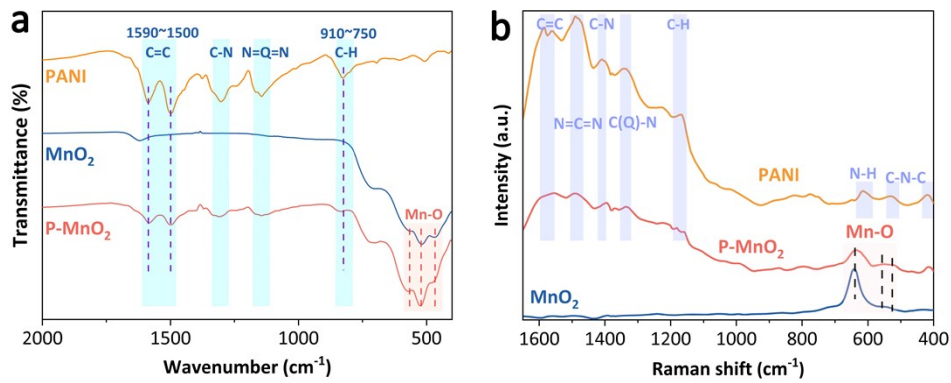


Fig. S5 (a) FTIR and (b) Raman spectra of PANI, MnO₂, P-MnO₂ cathodes, respectively.

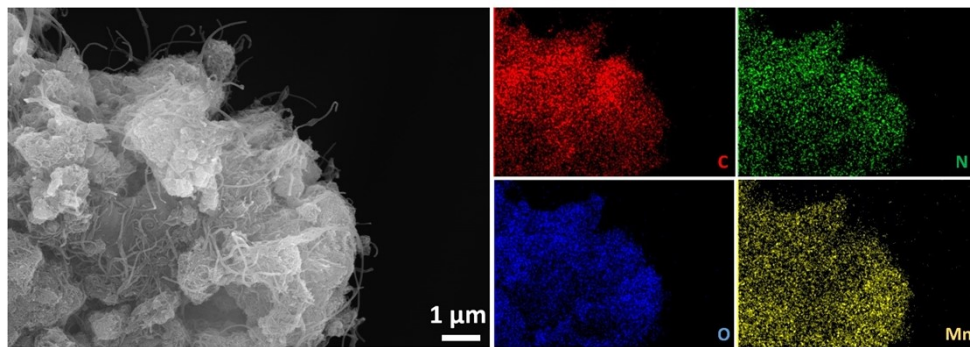


Fig. S6 SEM image of P-MnO₂ and corresponding elemental mapping images of C, N, O, Mn, respectively.

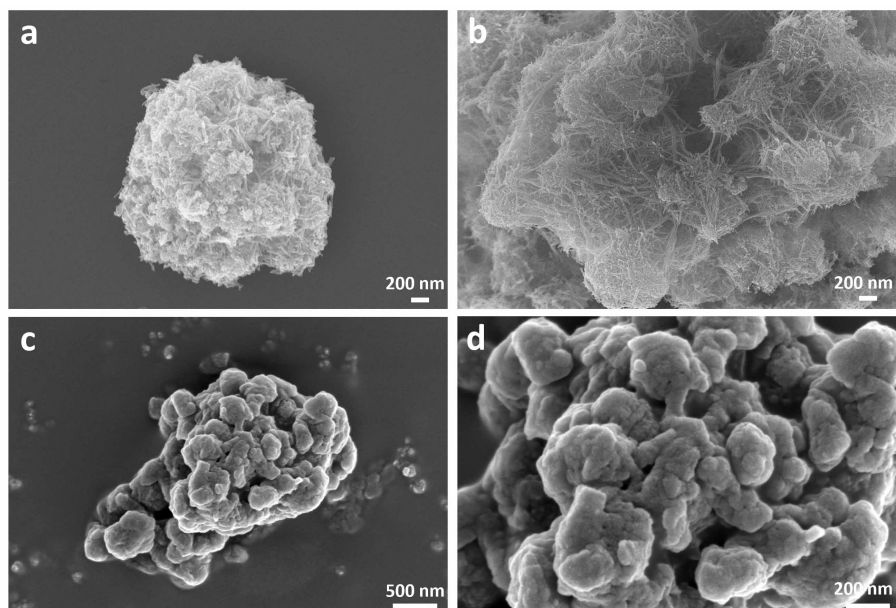


Fig. S7 SEM images of (a, b) MnO₂ and (c, d) PANI at different magnifications, respectively.

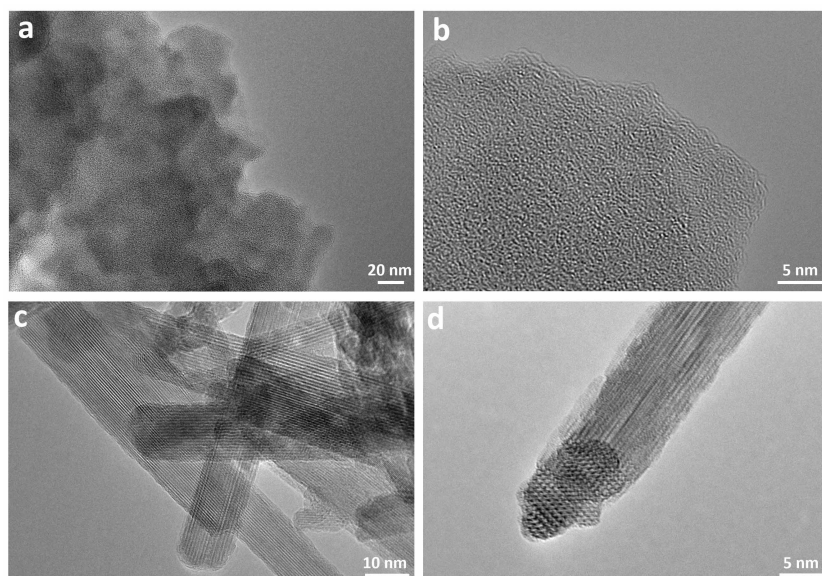


Fig. S8 HRTEM images of (a, b) PANI and (c, d) MnO₂ at different magnifications, respectively.

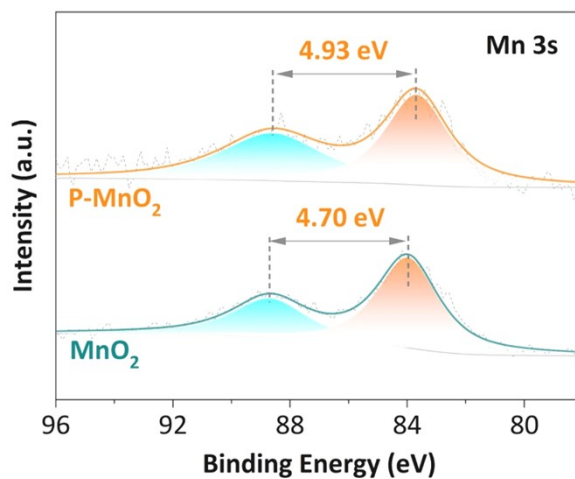


Fig. S9 Mn 3s XPS spectra of MnO₂ and P-MnO₂, respectively.

The average oxidation state (AOS) of P-MnO₂ is approximately 3.40, as calculated from the energy difference in splitting peaks (ΔE_s) in Mn 3s X-ray photoelectron spectroscopy (XPS) spectra ($\text{AOS} = 8.956 - 1.126 \Delta E_s$), which is lower than the average valence state 3.66 of the reference sample MnO₂ (**Fig. S9**).^[7] Such decreased Mn valence in P-MnO₂ implied the reduction of MnO₂ caused by its interaction with PANI chains. Thus, P-MnO₂ cathode exhibits the decreased electrostatic charge interaction for the high-rate and fast-charging Zn-Mn batteries.

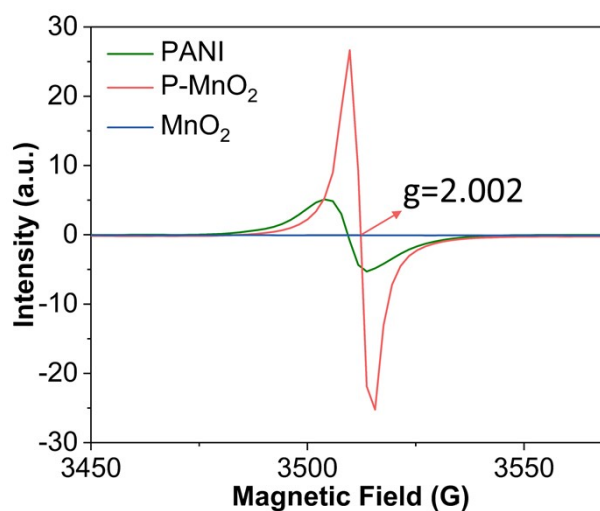


Fig. S10 Electron paramagnetic resonance (EPR) curves of PANI, MnO_2 and P-MnO_2 .

The electron paramagnetic resonance (EPR) curves of P-MnO_2 , PANI and MnO_2 were collected to illustrate the origin of oxygen vacancy (**Fig. S10**).^[8] Notably, the intensity of EPR gradually enhanced along with an increase in the concentration of oxygen vacancy. As a result, the EPR intensity of P-MnO_2 is significantly higher than that of PANI and MnO_2 , suggesting the oxygen vacancy formation caused by the PANI layer in P-MnO_2 .

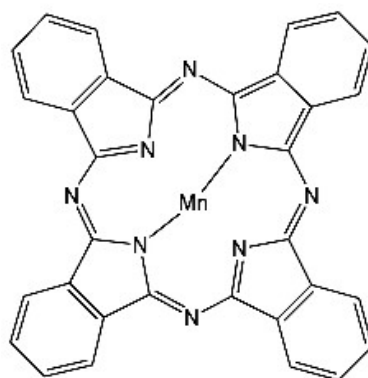


Fig. S11 The structure of manganese phthalocyanine (MnPc).

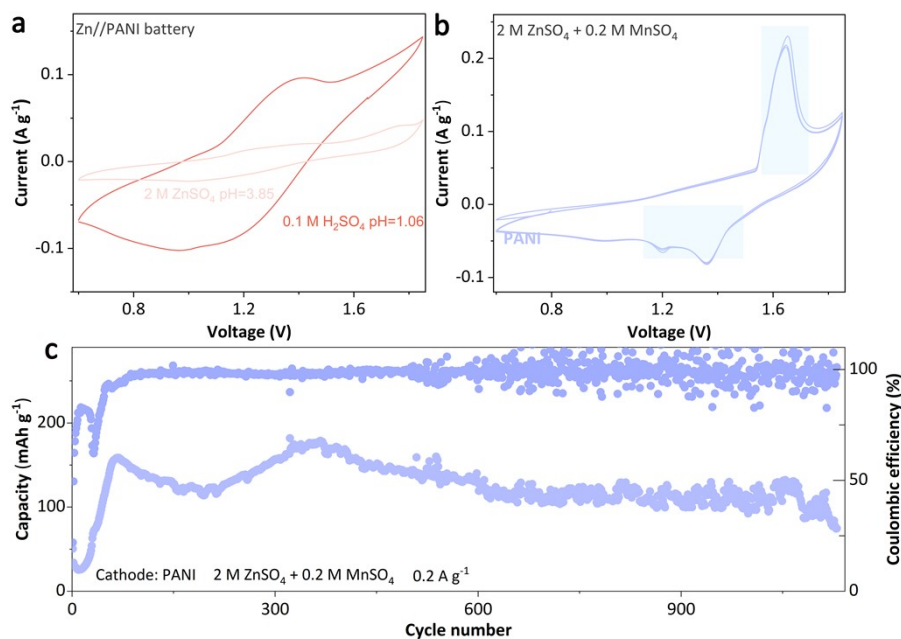


Fig. S12 (a) CV curves of Zn//PANI battery in 2 M ZnSO₄ and 0.1 M H₂SO₄ electrolytes, respectively. (b) CV curves, (c) cycling performance at 0.2 A g⁻¹ of Zn//PANI in 2 M ZnSO₄ + 0.2 M MnSO₄ electrolyte. (The cathode material is composed of PANI, CNTs and PVDF in a ratio of 7:2:1).

As shown in **Fig. S12a**, the obviously enhanced redox peaks indicated the preferred H⁺ storage chemistry of PANI cathode in 0.1 M H₂SO₄ electrolyte. Furthermore, the H⁺-rich PANI layer can greatly boost the reversible electrodeposition and dissolution of MnO₂ from electrolytic Mn²⁺, which can be confirmed by the newly appeared redox peaks of MnO₂ (**Fig. S12b, c**).

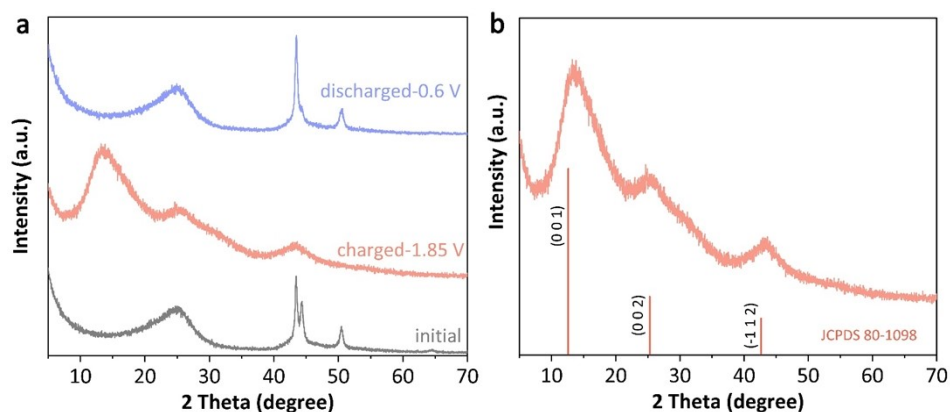


Fig. S13 (a) *Ex-situ* XRD patterns of PANI electrode in Zn//PANI battery using a 2 M ZnSO₄ + 0.2 M MnSO₄ electrolyte. (b) XRD patterns of PANI electrode at fully charged state. (The cathode material is composed of PANI, super P and PVDF in a ratio of 6:3:1).

At fully charged state, the observation of characteristic peaks onto PANI surface belonged to MnO₂ (JCPDS 80-1098) (**Fig. S13b**). Subsequently, these peaks disappeared during discharging process (**Fig. S13a**). Thus, “proton-rich” PANI provides effective deposition sites to boost the reversibility of electrolytic MnO₂/Mn²⁺ reaction, thus realizing the dual-energy storage mechanism for high-capacity and long-lifespan P-MnO₂ cathode.

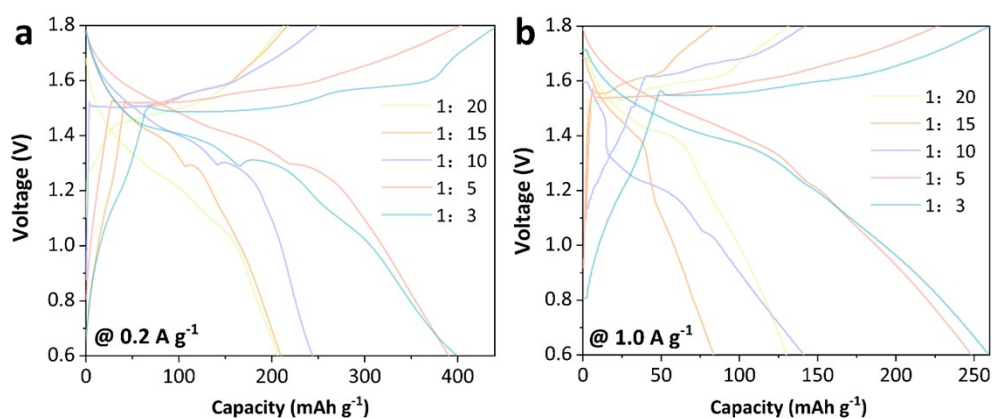


Fig. S14 Charge-discharge curves of P-MnO₂ cathodes with different mass ratios of PANI and MnO₂ at (a) 0.2 and (b) 1.0 A g⁻¹, respectively.

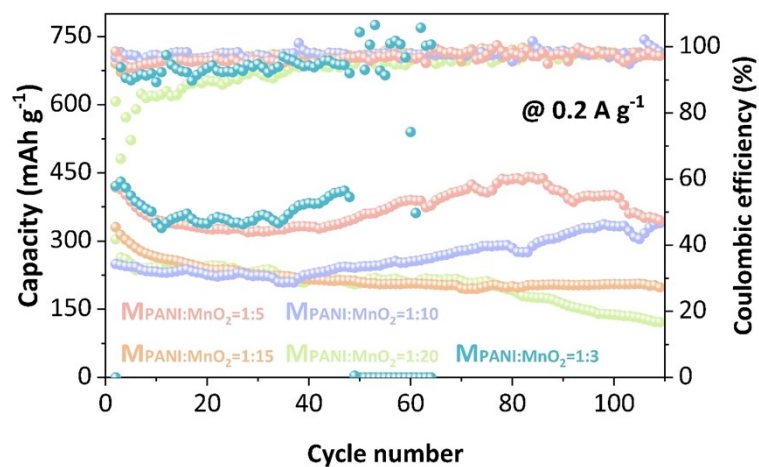


Fig. S15 The cycling performance of P-MnO₂ cathodes based on different mass ratios of PANI and MnO₂ hosts.

With the regulation of PANI addition mass, we found that PANI and MnO₂ with the mass ratio of 1:5 can realize the optimized capacity and cycling stability in P-MnO₂ cathodes (**Fig. S14, S15**).

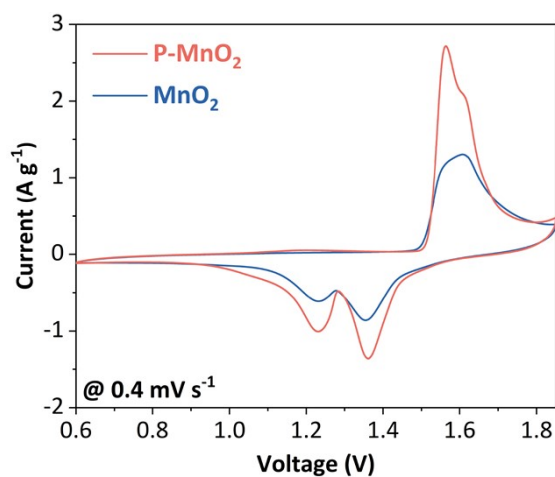


Fig. S16 CV curves of MnO₂ and P-MnO₂ cathodes in 2 M ZnSO₄ + 0.2 M MnSO₄.

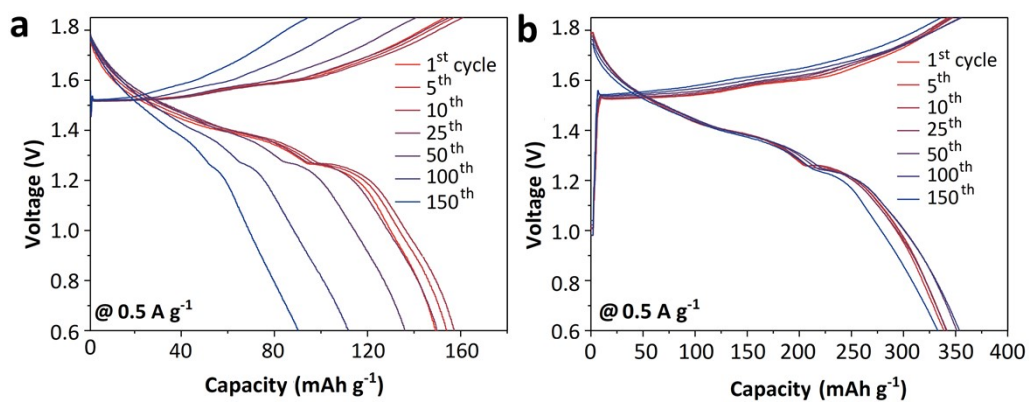


Fig. S17 GCD curves of (a) MnO_2 and (b) P-MnO_2 after different cycles at 0.5 A g^{-1} .

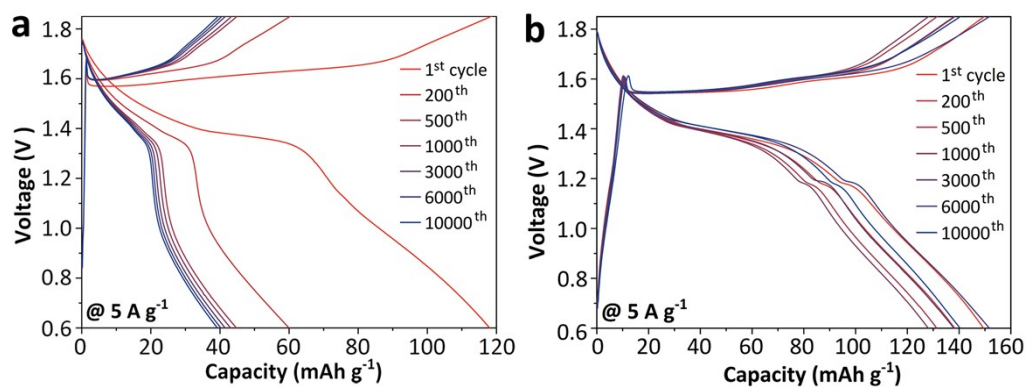


Fig. S18 CD curves of (a) MnO_2 and (b) P-MnO_2 after battery cycling at 5.0 A g^{-1} .

Compared with bare MnO_2 cathodes, P-MnO_2 cathode exhibits repeatable CD profiles along with negligible capacity decay, suggesting the excellent cycling stability caused by the core-shell structure of P-MnO_2 hosts (**Fig. S17, S18**).

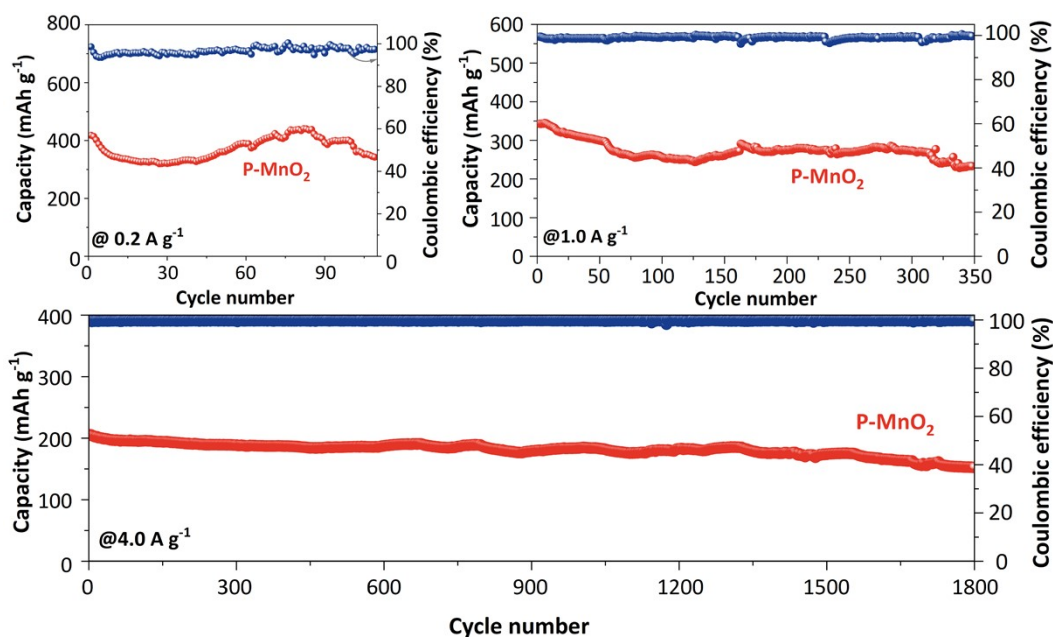


Fig. S19 The cycling performance of P-MnO₂ at different current densities.

As shown in **Fig. S19**, P-MnO₂ cathode displayed excellent cycling stability and high capacity reservation at 0.2, 1.0 and 4.0 A g⁻¹.

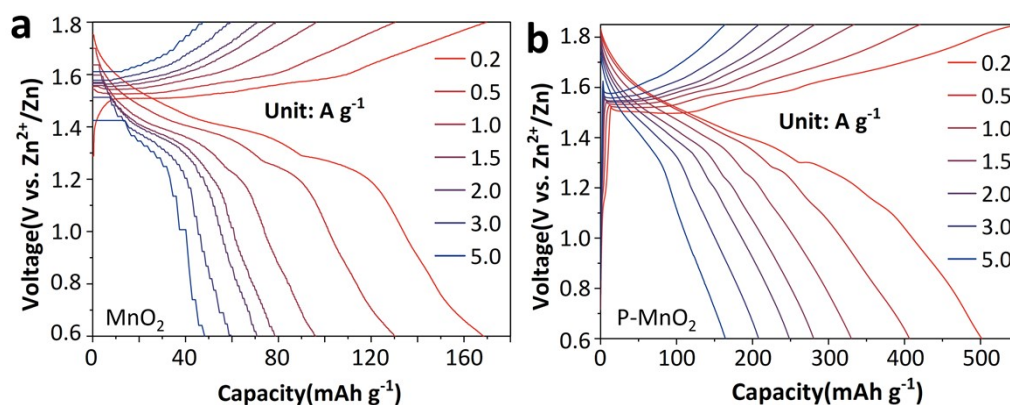


Fig. S20 Rate performances of (a) MnO₂ and (b) P-MnO₂, respectively.

Compared with bare MnO₂, P-MnO₂ cathode exhibits superior rate performance induced by the conductive PANI layer with well proton reservation capability, boosting the charge transfer and diffusion kinetics (**Fig. S20**).

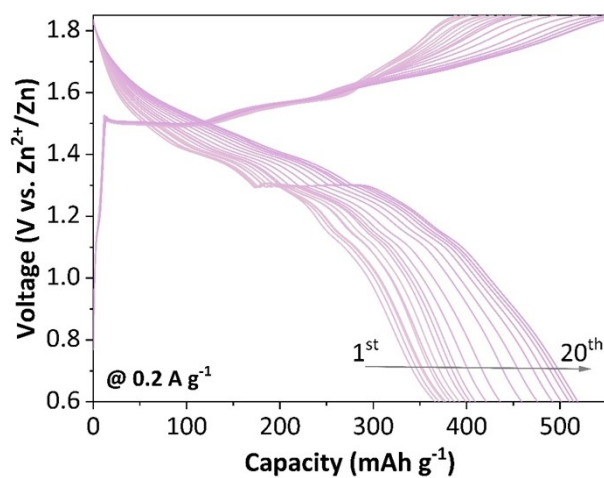


Fig. S21 Charge-discharge profiles of P-MnO₂ during the first 20 cycles at a current density of 0.2 A g⁻¹, illustrating the activation of MnO₂/Mn²⁺ reaction.

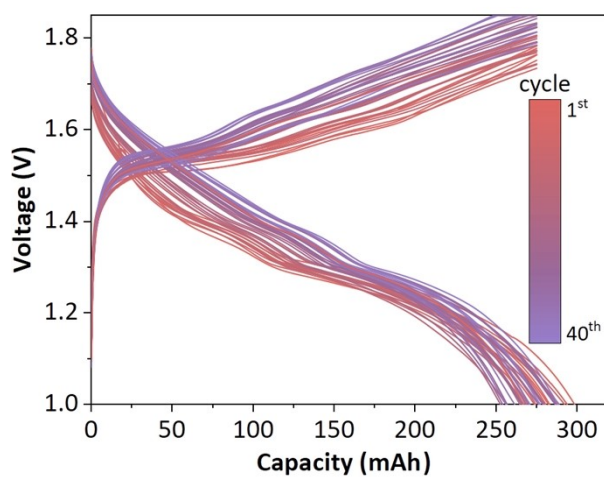


Fig. S22 Charge-discharge profiles of Zn//P-MnO₂ pouch cell after the first 40 cycles at a current of 50 mA (Thereinto the active mass of P-MnO₂ is 2 g).

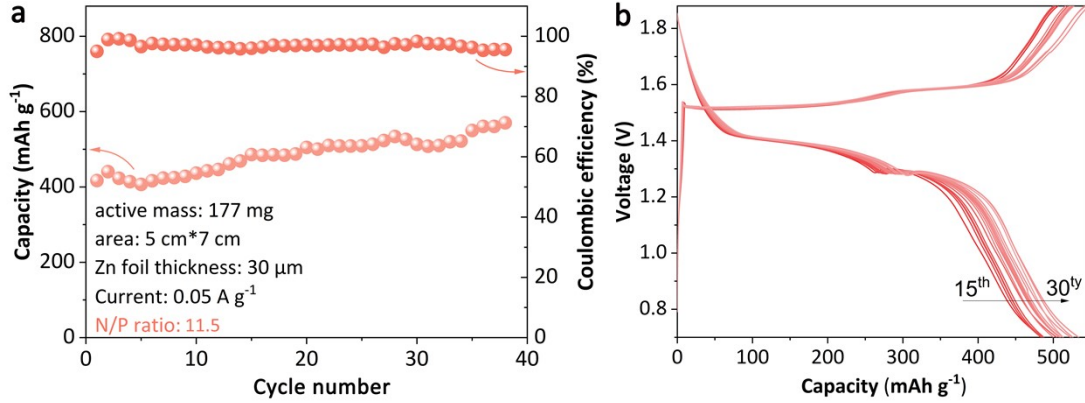


Fig. S23 (a) Cycling performance and (b) Charge-discharge profiles of the pouch cell at low N:P ratio of 4.9:1.

N/P ratio refers to the excess capacity of the anode over the cathode under the same conditions. Q_{NE} , Q_{PE} , q_{NE} , q_{PE} , m_{NE} , m_{PE} represents the anode capacity, cathode capacity, anode theoretical capacity, cathode theoretical capacity, anode mass and cathode mass, respectively.

$$\text{Equation 1: } R_{N/P} = Q_{NE}/Q_{PE} = (820 \text{ mAh g}^{-1} \times 18.5 \text{ g cm}^{-2} \times 2) / (520 \text{ mAh g}^{-1} \times 5.06 \text{ g cm}^{-2}) = 11.5$$

As shown in **Fig. 3e**, the Zn pouch cell with the total capacity of 275 mAh was fabricated by the single-layer P-MnO₂ cathode (23.5 mg cm⁻²) and two-layer 60-μm-thick Zn anode (33 mg cm⁻²). Based the following Equation 2, the negative/positive (N/P) ratio of the 275 mAh Zn//P-MnO₂ pouch cell was 4.43. And, the measured energy density (E_{energy}) of this cell based on the of P-MnO₂ and Zn foil mass (1.61 g + 3.44 g × 2) about 42.7 Wh kg⁻¹ according to the following Equation 3.

$$\text{Equation 2: } R_{N/P} = Q_{NE}/Q_{PE} = (820 \text{ mAh g}^{-1} \times 33 \text{ g cm}^{-2} \times 2) / (520 \text{ mAh g}^{-1} \times 23.5 \text{ g cm}^{-2}) = 4.43$$

$$\text{Equation 3: } E_{\text{energy}} = \text{Capacity} * \text{Average voltage} / \text{Active mass} = (0.275 \text{ Ah} \times 1.32 \text{ V} / 8.5 \times 10^{-3} \text{ kg}) = 42.7 \text{ Wh kg}^{-1}$$

Based the following Equation 4, the 1500 mAh battery employing a stacked design with three cathodes (23.5 mg cm⁻²) and four 60-μm-thick Zn foil anodes (33 mg cm⁻²), showing an N/P ratio of 2.95. And the measured energy density (E_{energy}) of this cell based on the of P-MnO₂ and Zn foil mass (1.61 g × 3 + 3.44 g × 4) about 106.5 Wh kg⁻¹ according to the following Equations 5.

$$\text{Equation 4: } R_{N/P} = Q_{NE} / Q_{PE} = (820 \text{ mAh g}^{-1} \times 33 \text{ g cm}^{-2} \times 4) / (520 \text{ mAh g}^{-1} \times 23.5 \text{ g cm}^{-2} \times 3) = 2.95$$

Equation 5: $E_{\text{energy}} = \text{Capacity} * \text{Average voltage} / \text{Active mass} = (1.5 \text{ Ah} \times 1.32 \text{ V}) / 1.86 \times 10^{-2} \text{ kg} = 106.5 \text{ Wh kg}^{-1}$

The above calculated results demonstrated that precise control of N/P ratio and optimized stacking process is essential for the maximize the electrode materials utilization to realize the target of sufficient Zn inventory and high energy density.

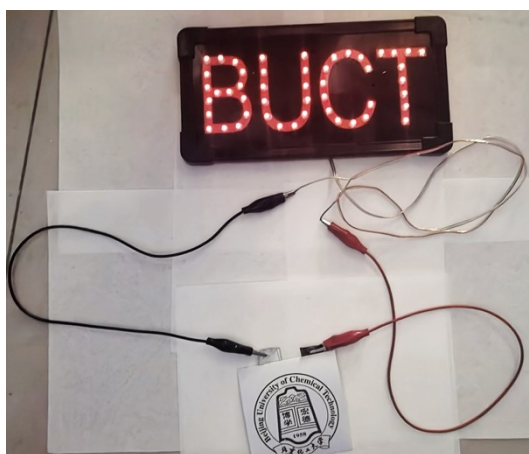


Fig. S24 LED device powered by a Zn//P-MnO₂ pouch battery.

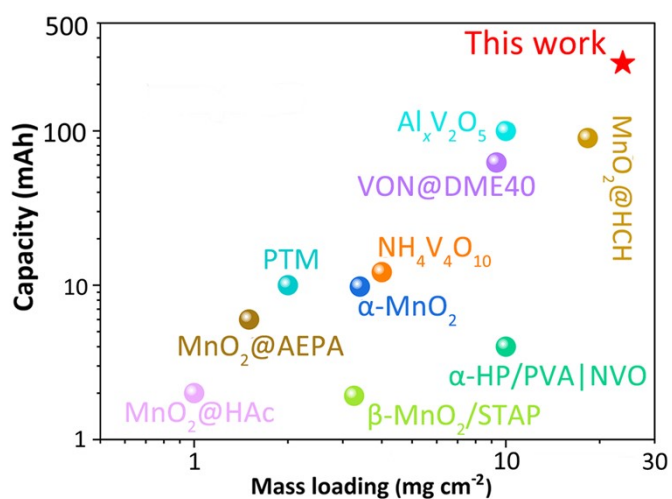


Fig. S25 Comparisons of Zn//P-MnO₂ pouch cells based on 23.5 mg cm⁻² P-MnO₂ cathode with other reported Zn pouch cells.



Fig. S26 Display diagram of large-scale production application of P-MnO₂.

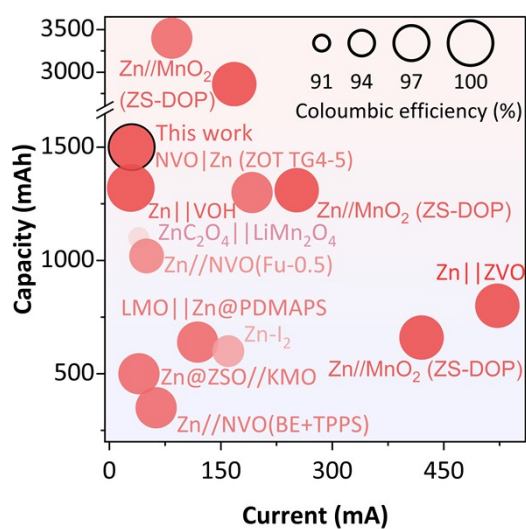


Fig. S27 Electrochemical performance comparison of P-MnO₂ and reported MnO₂ cathodes in pouch cell.

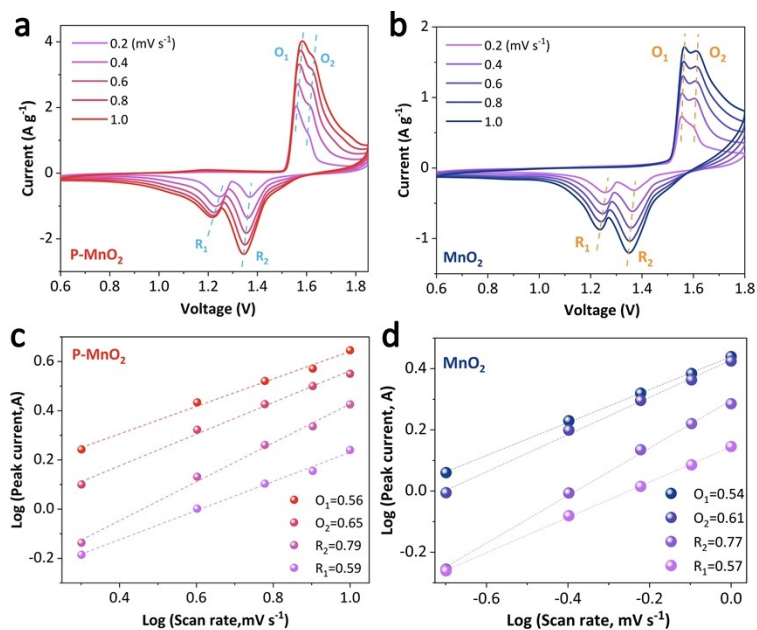


Fig. S28 CV profiles and calculated b -values of (a, c) P-MnO₂ and (b, d) MnO₂ at different scanning rates, respectively.

Notably, the CV profiles remain in excellent shape at different scan rates, indicating the fast reaction kinetics of P-MnO₂ cathode. Compared with bare MnO₂, P-MnO₂ cathode exhibits higher b values, indicating the boosted reaction kinetics induced by the regulated organic-inorganic interfacial engineering.

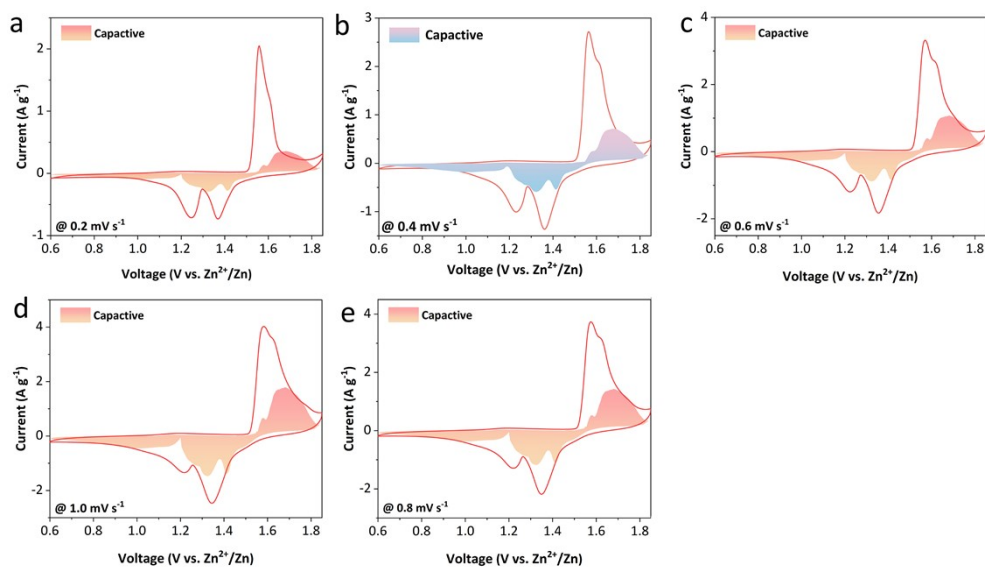


Fig. S29 The percentage of capacitance contribution at various scan rates of P-MnO₂.

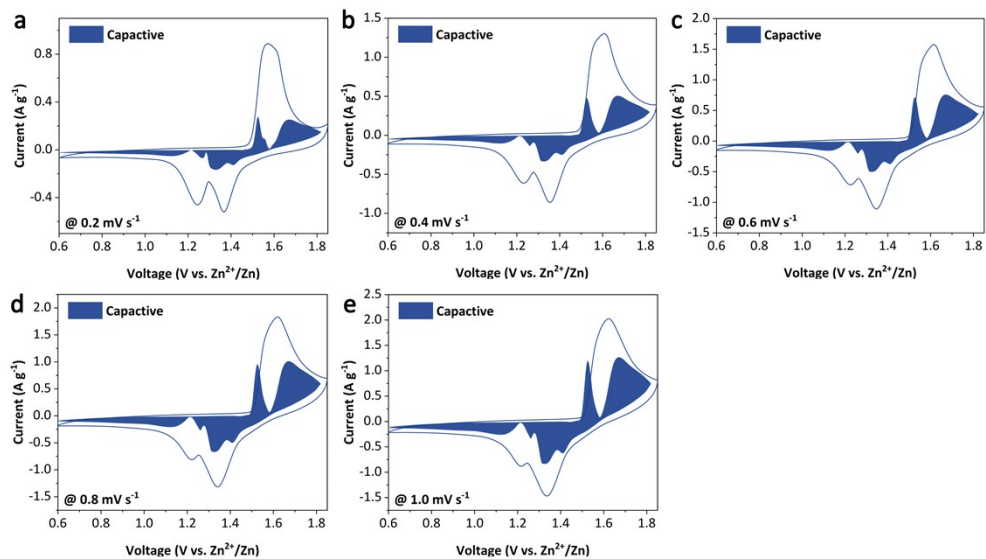


Fig. S30 The percentage of capacitance contribution at various scan rates of MnO_2 .

Specifically, the surface-controlled CV profiles of P- MnO_2 and MnO_2 were shown in **Fig. S29** and **S30**, respectively, suggesting the boosted reaction kinetics of P- MnO_2 contributed to the organic-inorganic interfacial design.

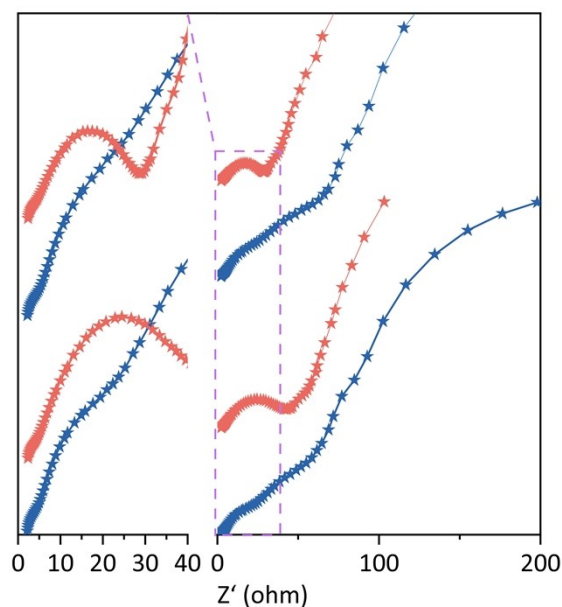


Fig. S31 EIS Nyquist plots of PANI- MnO_2 electrode without CNTs.

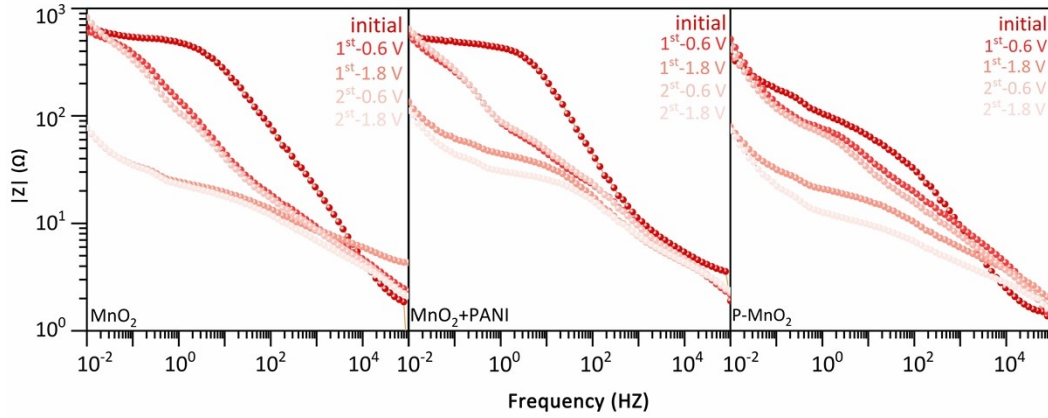


Fig. S32 EIS bode plots of MnO_2 , PANI- MnO_2 , and P- MnO_2 .

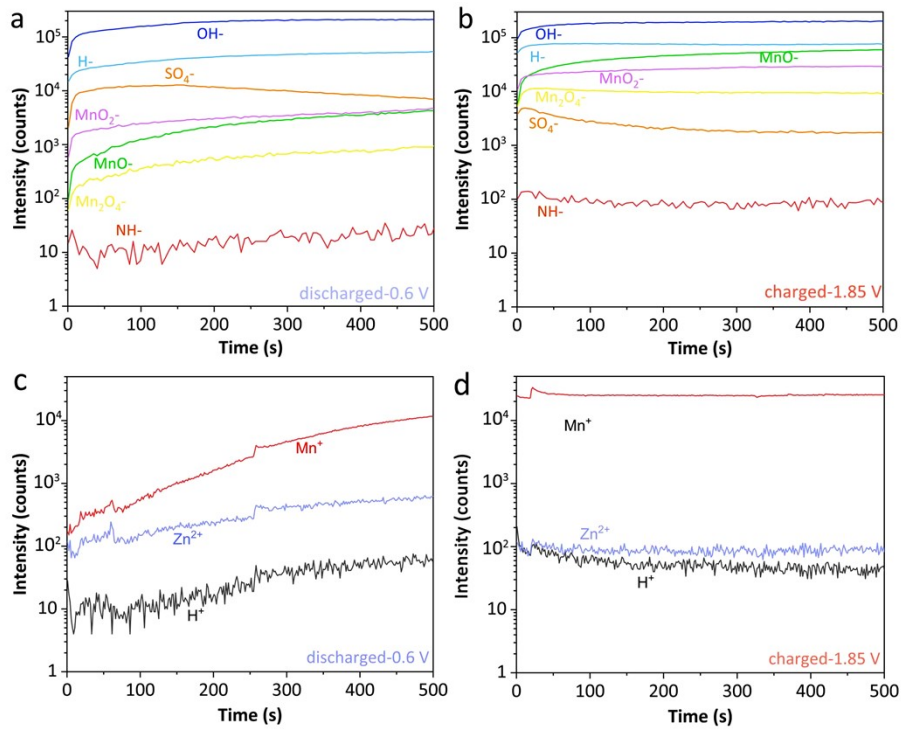


Fig. S33 Depth profiling TOF-SIMS analyses of P- MnO_2 cathode at fully discharged (a, c) and charged (b, d) states after 25 cycles.

At the fully discharged state, protons insertion into the bulk of P- MnO_2 leads to an increase in H^+ and NH^- content. Surprisingly, when charged to 1.85V, there is still a notable enhancement in the content of H^+ and NH^- within P- MnO_2 , as illustrated in **Fig. S33**. The results indicate that

PANI is able to modulate the microenvironment surrounding MnO_2 . It facilitates proton storage and promotes the reversible dissolution/deposition of $\text{MnO}_2/\text{Mn}^{2+}$ reaction.

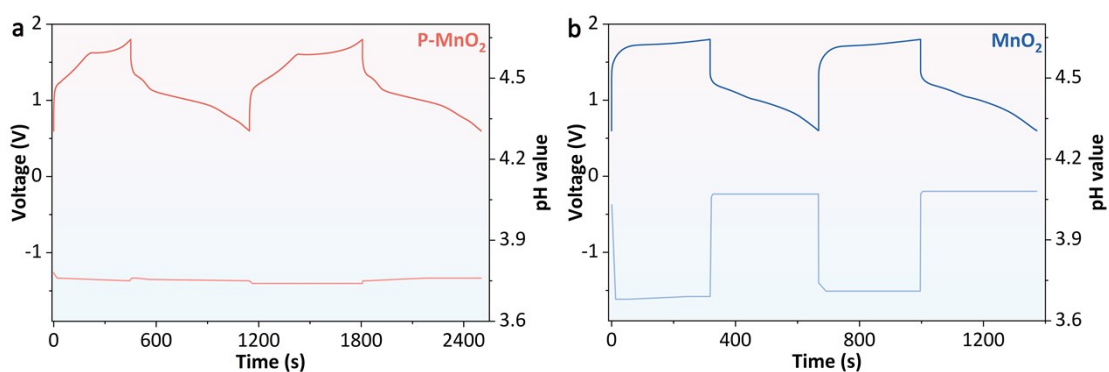


Fig. S34 *In-situ* PH value detection of the electrolytes. (a) P-MnO₂, (b) MnO₂. (Near the cathode of full cell using 2 M ZnSO₄ + 0.2 M MnSO₄ as the baseline electrolyte, and the mass loading and area of cathodes are same.)

As revealed in **Fig. S34**, the cathode material contains PANI, which exhibits exceptional pH buffering capacity. It further emphasizes that PANI can effectively store and release protons as shown in **Fig. S33**, thereby serving a crucial role in pH buffering.

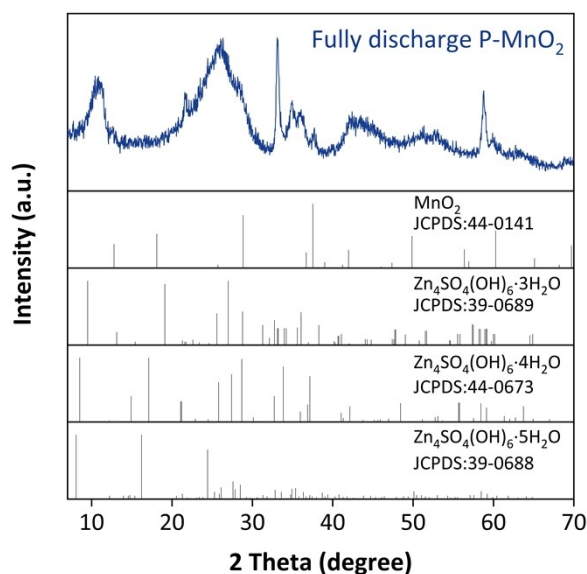


Fig. S35 XRD patterns of P-MnO₂ cathode at fully discharged state.

Meanwhile, new diffraction peaks belonging to Zn₄SO₄(OH)₆·4H₂O (ZSH) reversibly appear in the first two discharged states of P-MnO₂ cathode (**Fig. S35**). And the emergence of ZSH can be attributed to H⁺ insertion into the cathode resulting in surface accumulation of OH⁻, which reacts with Zn²⁺, SO₄²⁻ and H₂O to form ZSH during battery discharging process.^[9]

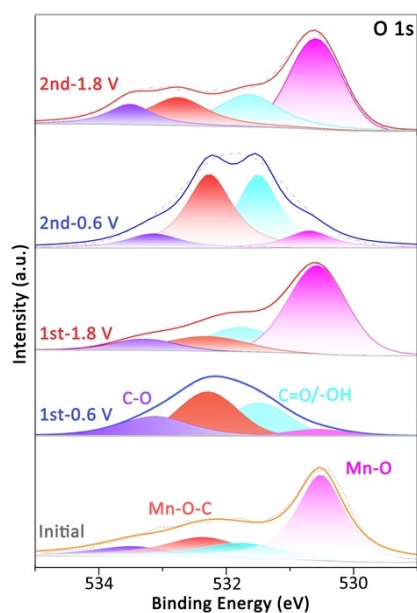


Fig. S36 XPS spectra of O 1s at different voltage states in P-MnO₂ electrode.

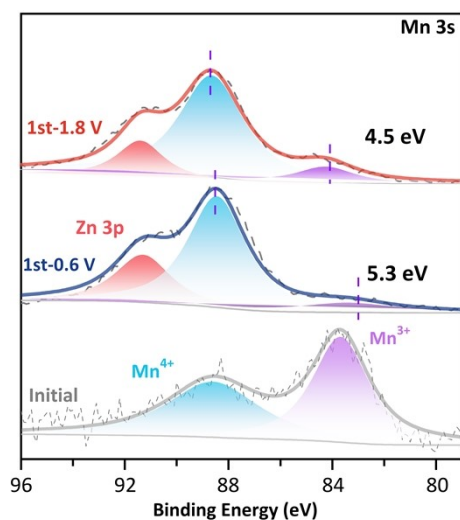


Fig. S37 XPS spectra of Mn 3s at different voltage states in P-MnO₂ electrode.

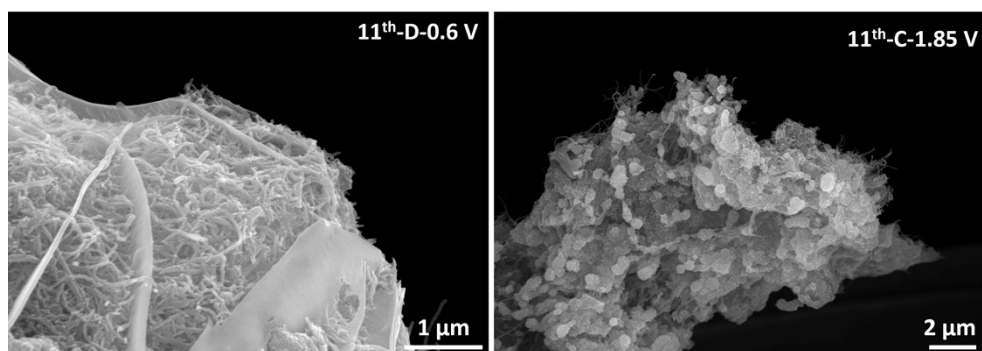


Fig. S38 SEM images of P-MnO₂ at fully discharged (left) and charged (right) states after 11 cycles.

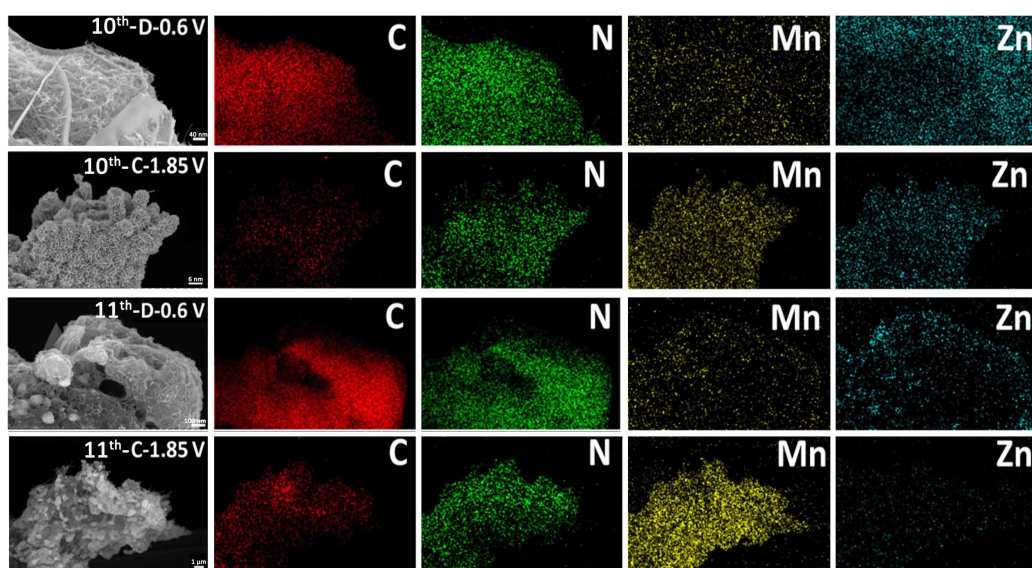


Fig. S39 SEM element mapping images of P-MnO₂ at fully discharged and charged states after 10 and 11 cycles.

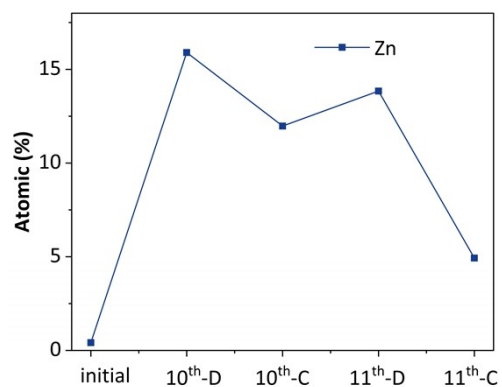


Fig. S40 Variation of Zn atomic percentage on the surface of P-MnO₂ cathode throughout the battery cycle.

The variation of Zn element during 10th and 11th cycles further confirms the reversible formation of ZSH along with proton insertion chemistry (**Fig. S39, S40**).

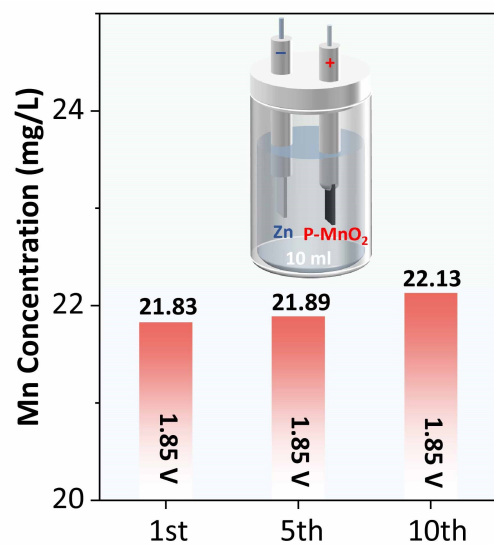


Fig. S41 Mn concentrations in the electrolytes at 1.85 V states.

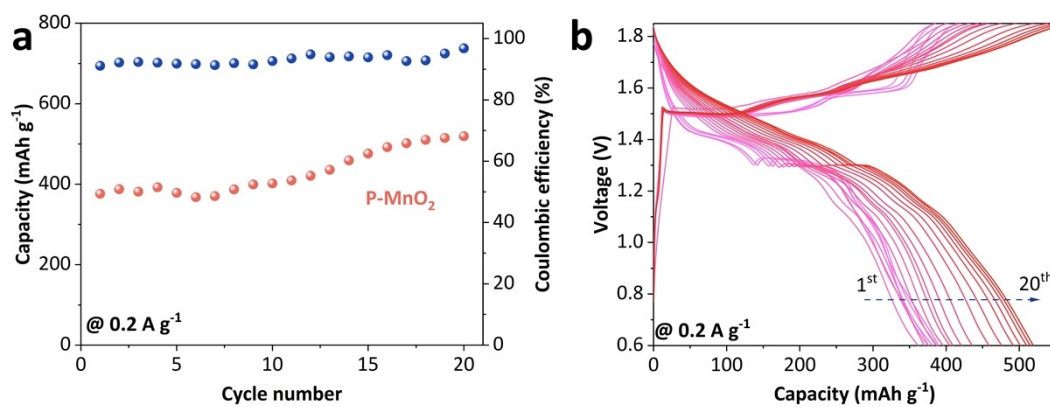


Fig. S42 (a) Cycle performance and (b) CD profiles of Zn//P-MnO₂ battery during the first 20 cycles.

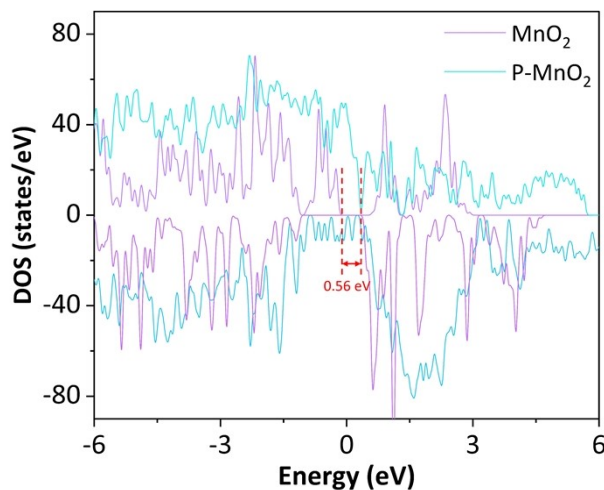


Fig. S43 The calculated total density of states (TDOS) of P-MnO₂ and MnO₂.

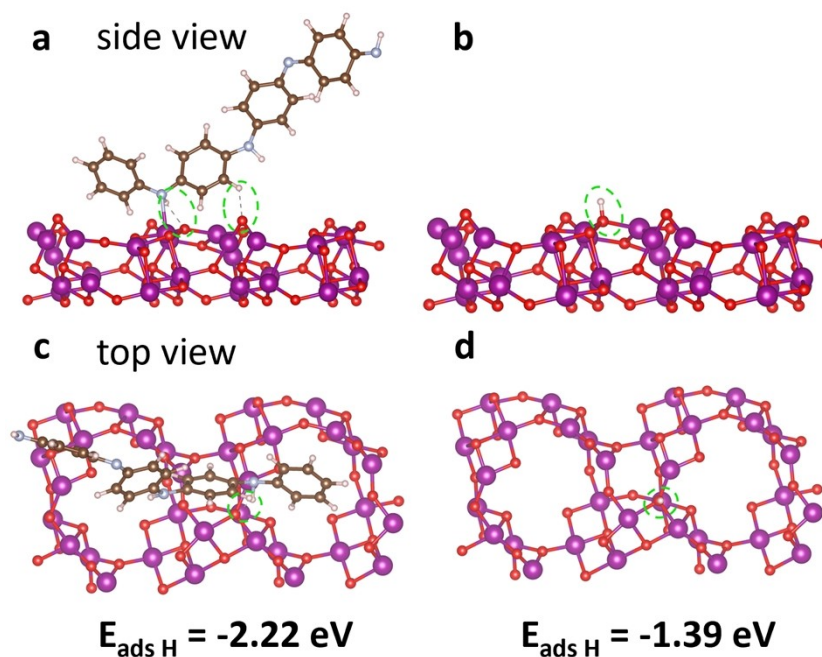


Fig. S44 Schematic diagram illustrating the adsorption energy of H⁺ ions on the surface of (a, c) P-MnO₂, along with the corresponding diagrams for (b, d) MnO₂.

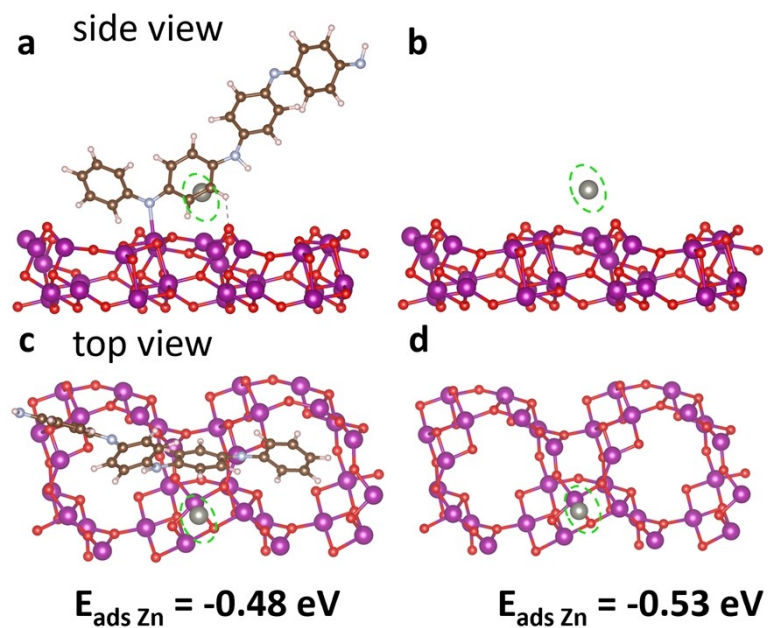


Fig. S45 Schematic representation of the adsorption energy Zn^{2+} ion on the surface of (a, c) P- MnO_2 , together with the relevant illustrations for (b, d) MnO_2 .

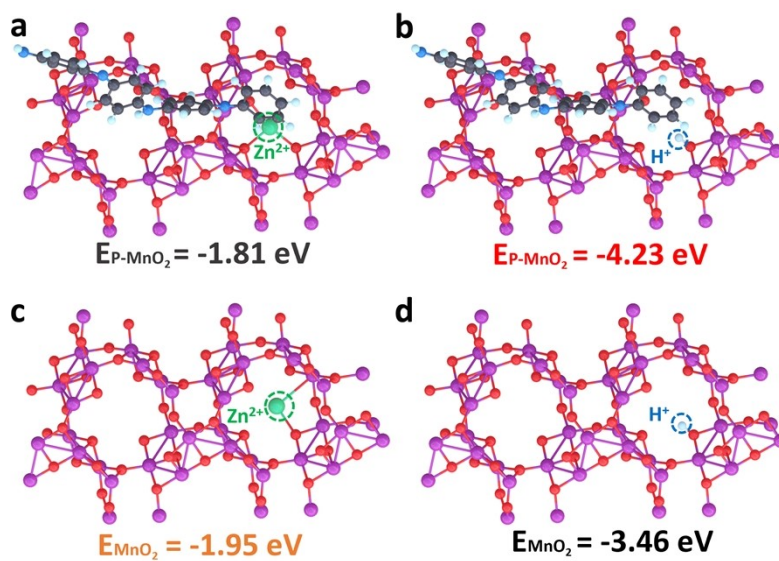


Fig. S46 Schematic diagram of (a) Zn^{2+} and (b) H^+ ion insertion energy in tunnel-type P- MnO_2 , respectively. Schematic diagram of (c) Zn^{2+} and (d) H^+ ion insertion energy in tunnel-type MnO_2 , respectively.

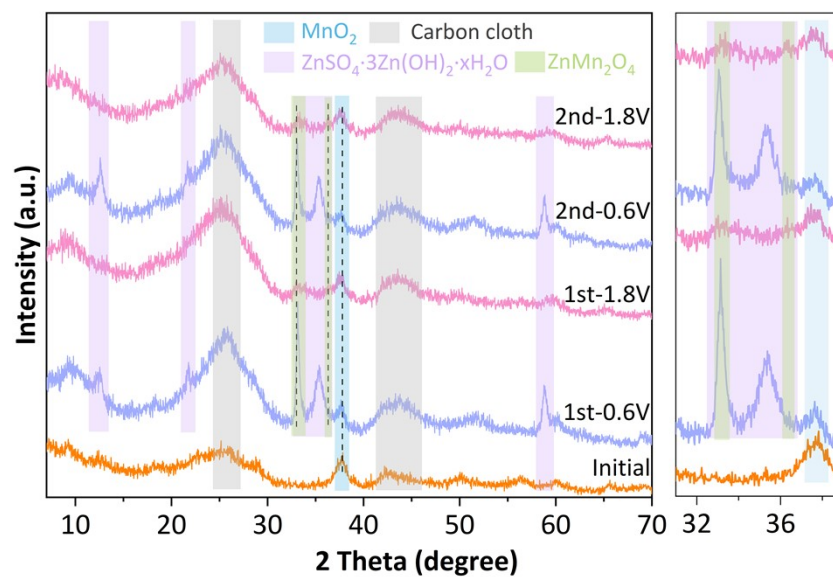


Fig. S47 *Ex-situ* XRD patterns of MnO₂ cathode.

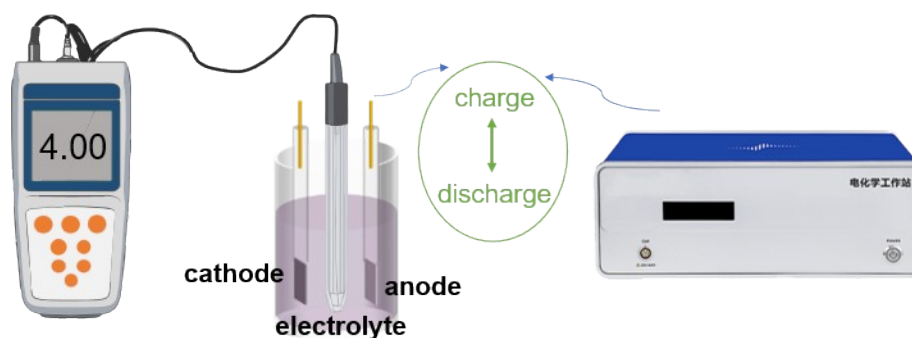


Fig. S48 Schematic diagrams of *in situ* pH monitoring.

The *in-situ* pH monitoring experiment was conducted in a sealed electrochemical cell containing 40 mL of 2 M ZnSO₄ + 0.2 M MnSO₄ aqueous electrolyte, the installation diagram is shown below (**Fig. S48**). A symmetric two-electrode configuration was assembled using pre-treated cathode and anode materials (2×3 cm² geometric area each), along with a pre-calibrated pH probe (standard buffers: pH 4.01, 7.01, and 10.01). After 60 minutes of system equilibration under quiescent conditions at 25.0±0.5°C, galvanostatic charge-discharge tests were performed at 0.5 A g⁻¹ with continuous magnetic stirring (50 rpm). Throughout the experiment, electrolyte

pH evolution was monitored using a traceable pH meter (± 0.01 resolution) with 30-second sampling intervals, while simultaneously recording voltage-time profiles via electrochemical workstation to ensure data synchronization. Special care was taken to maintain constant temperature and eliminate gas bubble interference at the electrode surfaces.

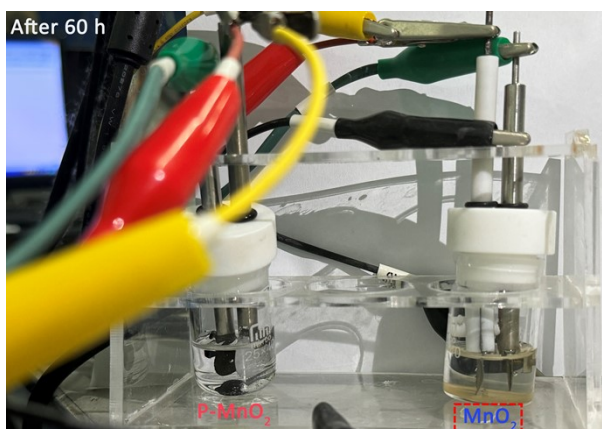


Fig. S49 Digital photographs of ICP test device of P-MnO₂ (left), MnO₂ (right) cathode materials.

After 45 cycles at full charged state, compared with P-MnO₂, the Mn²⁺ concentration matched with bare MnO₂ cathode has a significantly decrease (**Table S3**). And combined with **Fig. S49**, it suggests the structural collapse of bare MnO₂ without the PANI layer protection.

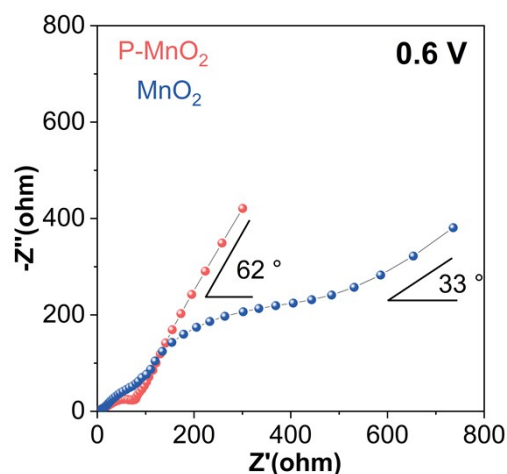


Fig. S50 The EIS Nyquist plots of P-MnO₂ and MnO₂ cathodes at the 1st fully discharged state.

Fig. S50 can well support the conclusion that P-MnO₂ featured with the proton-rich PANI layer facilitates proton transport while selectively blocks Zn²⁺ insertion into MnO₂ bulk. Specifically, P-MnO₂ cathode deviates from the ideal semi-infinite diffusion behavior (Warburg slope=1) to the finite space diffusion process (Warburg slope=1.88) at the fully discharged state. More importantly, the finite space diffusion process in P-MnO₂ is in agreement with the reaction mechanism of boosted H⁺ insertion (battery-like behavior) and blocked Zn²⁺ diffusion (capacitive behavior) attributing to the proton-rich PANI layer. In contrast, the Warburg slope of bare MnO₂ cathode is about 0.65, much lower than that of P-MnO₂ cathode. Such sluggish charge diffusion kinetics in bare MnO₂ can be attributed to the generation of ZnMn₂O₄ and Zn₄SO₄(OH)₆·xH₂O caused by the Zn²⁺ and proton insertion, respectively, which significantly increased the interfacial charge transfer resistance for inferior rate performance of MnO₂.

Table S1. Curvefit parameters^a for Mn K-edge EXAFS spectra of P-MnO₂.

Sample	Path	N	Reff/Å	R/Å	σ ² /Å ²	E ₀ /eV
P-MnO ₂	Mn-O	3 ^b	1.90	1.91(2)	0.003(2) ^c	9(1)
	Mn-N	0.2(3)	1.91	1.93(2)	0.003(2) ^c	
	Mn-Mn1 (second shell)	3 ^b	2.88	2.89(8)	0.03(1)	

^a S₀² was fixed as 1.0. Data ranges: 2.0 < k < 10.0 Å⁻¹, 1.0 < R < 3.0 Å. The number of variable parameters is 7. out of a total of 9.9 independent data points. R factor for this fit is 2.1 %. The

various paths in the Table are generated from the Feff calculations of P-MnO₂ structure cif file. ^b These coordination numbers were constrained as $N(\text{Mn-O}) = 3$ and $N(\text{Mn-N}) = 3$ based on the crystal structure. ^c The Debye-Waller factors were constrained as $\sigma^2(\text{Mn-O}) = \sigma^2(\text{Mn-N})$ for decreasing the correlation (or reducing the number of variables).

Table S2. ICP results of electrolytic Mn concentrations at fully charged states in Zn//P-MnO₂ batteries.

Sample name	Dilution ratio	C (mg/ml)	C ₀ (mg/ml)
1 st -1.85 V	400	21.83	8731.6
5 th -1.85 V	400	21.89	8756.8
10 th -1.85 V	400	22.13	8851.6

(Test element is Mn, C is instrument reading concentration, Dilution ratio is 400, C₀ is the concentration of the original sample solution.)

Table S3. ICP results of electrolytic Mn concentrations at fully charged states in Zn//MnO₂ and Zn//P-MnO₂ batteries after 82 hours.

Sample	C ₁ /mg·L ⁻¹	C ₂ /mg·L ⁻¹	C ₃ /mg·L ⁻¹	C _{average} /mg·L ⁻¹
initial	7645	7642	7640	7642.3
MnO ₂	7589	7583	7583	7585.7
P-MnO ₂	7638	7642	7645	7641.7

(Test element is Mn, C₁, C₂, C₃ is instrument reading concentration for three times, respectively. C_{average} is the average concentration of the original sample solution.)

Table S4. Energy storage mechanism and battery performance comparisons of P-MnO₂ and other reported Mn-based cathodes.

Cathode	Reaction mechanism	Rate performance	Cycling performance
PANI/ MnO ₂ ^[10]	H ⁺ and Zn ²⁺ co-insertion	280 mAh g ⁻¹ at 0.2 A g ⁻¹ 125 mAh g ⁻¹ at 2.0 A g ⁻¹	90% capacity retention (200 cycle at 0.2 A g ⁻¹) 90% capacity retention (5000 cycle at 2.0 A g ⁻¹)
PEDOT- MnO ₂ ^[11]	H ⁺ and Zn ²⁺ co-insertion	344 mAh g ⁻¹ at 0.2 A g ⁻¹ 121 mAh g ⁻¹ at 2.0 A g ⁻¹	100% capacity retention (100 cycle at 0.2 A g ⁻¹) 100% capacity retention (1500 cycle at 2.0 A g ⁻¹)
Al-MnO ₂ ^[12]	H ⁺ and Zn ²⁺ co-insertion	328 mAh g ⁻¹ at 0.2 A g ⁻¹	98% capacity retention (200 cycle at 0.2 A g ⁻¹)
S-MnO ₂ ^[13]	H ⁺ and Zn ²⁺ co-insertion	324 mAh g ⁻¹ at 0.2 A g ⁻¹ 150 mAh g ⁻¹ at 3.0 A g ⁻¹	100% capacity retention (100 cycle at 0.2 A g ⁻¹) 90% capacity retention (1000 cycle at 3.0 A g ⁻¹)
MnO ₂ /PPy ^[14]	Zn ²⁺ insertion	256 mAh g ⁻¹ at 0.1 A g ⁻¹	100% capacity retention (50 cycle at 0.1 A g ⁻¹)
Na _{0.55} Mn ₂ O ₄ • 1.5H ₂ O ^[15]	H ⁺ and Zn ²⁺ co-insertion	100 mAh g ⁻¹ at 2.0 A g ⁻¹	70% capacity retention (10,000 cycle at 2.0 A g ⁻¹)
C@PODA/ MnO ₂ ^[16]	H ⁺ and Zn ²⁺ co-insertion	140 mAh g ⁻¹ at 2.0 A g ⁻¹	89.3% capacity retention (2000 cycle at 2.0 A g ⁻¹)
BiO/MnO ₂ ^[7]	H ⁺ and Zn ²⁺ co-insertion	113 mAh g ⁻¹ at 2.0 A g ⁻¹	100% capacity retention (2000 cycle at 2.0 A g ⁻¹)
MnO ₂ @ AEPA ^[17]	H ⁺ and Zn ²⁺ co-insertion	223 mAh g ⁻¹ at 0.5 A g ⁻¹ 146 mAh g ⁻¹ at 1.0 A g ⁻¹	100% capacity retention (200 cycle at 0.5 A g ⁻¹) 97% capacity retention (1700 cycle at 1.0 A g ⁻¹)
This work	H ⁺ insertion & MnO ₂ deposition	510 mAh g ⁻¹ at 0.2 A g ⁻¹ 140 mAh g ⁻¹ at 5.0 A g ⁻¹	99% capacity retention (100 cycle at 0.5 A g ⁻¹) 87% capacity retention (14,000 cycle at 5.0 A g ⁻¹)

Table S5. Battery performance comparisons of reported Zn pouch cells.

Cathode	Mass (mg/cm ²)	Capacity (mAh)	Area capacity (mAh/cm ²)	Cycle number
This work	23.7	275	10.86	110
NH ₄ V ₄ O ₁₀ ^[18]	4	12.15	1.08	1000
α-MnO ₂ ^[19]	3.4	9.8	0.612	100
β-MnO ₂ /STAP (MS-8) ^[20]	3.26	1.92	0.5	90
MnO ₂ @HAc ^[21]	1	2	2	100
MnO ₂ @HCH ^[22]	18.3	90	2.57	-
PTM ^[23]	2	10	0.25	40
MnO ₂ @AEPA ^[17]	1.5	6	0.3	110
α-HP/PVA NVO ^[24]	10	4	2	600
Al _x V ₂ O ₅ ^[25]	10	100	2	50
VOH@DME40 ^[26]	9.33	62.4	2.08	100

Table S6. Electrochemical performance comparisons of reported Zn pouch cells.

Cathode	Current (mA)	Capacity (mAh)	Coulombic efficiency (%)
This work	30	1500	100
	50	1280	100
	100	512	100

LMO Zn@PDMAPS ^[27]	118.8	640	98
NVO Zn(ZOT TG4-5) ^[28]	192	1300	98
Zn@ZSO//KMO ^[29]	39.72	500	98
Zn//NVO(BT+TPPS) ^[30]	62.8	350	98
ZnC ₂ O ₄ LiMn ₂ O ₄ ^[31]	39.6	1100	91.7
Zn//NVO(Fu-0.5) ^[32]	50	1020	96
Zn-I ₂ ^[33]	160	600	95
Zn ZVO ^[34]	522	800	99
Zn VOH ^[35]	28.8	1320	100

Reference

- [1] G. Kresse, J. Hafner, *Phys. Rev. B.*, **1993**, 47, 558.
- [2] G. Kresse, J. Hafner, *Phys. Rev. B.*, **1994**, 49, 14251.
- [3] J. P. Perdew, K. Burke, M. Ernzerhof, *Phys. Rev., Lett.* **1996**, 77, 3865.
- [4] G. Kresse, D. Joubert, *Phys. Rev. B.*, **1999**, 59, 1758.
- [5] P. E. Blöchl, *Phys. Rev. B.*, **1994**, 50, 17953.
- [6] S. Grimme, J. Antony, S. Ehrlich, H. J. Krieg, *Chem. Phys.*, **2010**, 132, 154104.
- [7] X. Zhao, F. Zhang, H. Li, H. Dong, C. Yan, C. Meng, Y. Sang, H. Liu, Y. Guo, S. Wang, *Energy Environ. Sci.*, **2024**, 17, 3629.
- [8] Z. Peng, Y. Huang, A. G. Bannov, S. Li, L. Tang, L. Tan, Y. Chen, *Energy Environ. Sci.*, **2024**, 17, 3384.
- [9] H. Chen, C. Dai, F. Xiao, Q. Yang, S. Cai, M. Xu, H. Fan, S. Bao, *Adv. Mater.*, **2022**, 34, e2109092.
- [10] J. Huang, Z. Wang, M. Hou, X. Dong, Y. Liu, Y. Wang, Y. Xia, *Nat. Commun.*, **2018**, 9, 2906.
- [11] H. Chen, W. Ma, J. Guo, J. Xiong, F. Hou, W. Si, Z. Sang, D. Yang, *J. Alloys Compd.*, **2023**, 932, 167688.
- [12] Y. Zhao, S. Zhang, Y. Zhang, J. Liang, L. Ren, H. Fan, W. Liu, X. Sun, *Energy Environ. Sci.*, **2024**, 17, 1279.
- [13] Y. Zhao, P. Zhang, J. Liang, X. Xia, L. Ren, L. Song, W. Liu, X. Sun, *Energy Storage Mater.*, **2022**, 47, 424.
- [14] J. Huang, X. Tang, K. Liu, G. Fang, Z. He, Z. Li, *Mater. Today Energy*, **2020**, 17, 100475.
- [15] Y. Xu, J. Zhu, J. Feng, Y. Wang, X. Wu, P. Ma, X. Zhang, G. Wang, X. Yan, *Energy Storage Mater.*, **2021**, 38, 299.

-
- [16] Y. Zhao, R. Zhou, Z. Song, X. Zhang, T. Zhang, A. Zhou, F. Wu, R. Chen, L. Li, *Angew. Chem. Int. Ed.*, **2022**, 61, e202212231.
- [17] X. Xiao, L. Zhang, W. Xin, M. Yang, Y. Geng, M. Niu, H. Zhang, Z. Zhu, *Small*, **2024**, 20, 2309271.
- [18] T. Wang, J. Jin, X. Zhao, X. Qu, L. Jiao, Y. Liu, *Angew. Chem. Int. Ed.*, **2024**, 63, e202412057.
- [19] Y. Hu, Z. Liu, L. Li, S. Guo, X. Xie, Z. Luo, G. Fang, S. Liang, *Natl. Sci. Rev.*, **2023**, 10, nwad220.
- [20] M. Chen, W. Liu, D. Ren, Y. An, C. Shu, S. Zhang, W. Liang, J. Sun, F. Kang, F. Jiang, *Adv. Funct. Mater.*, **2024**, 34, 2404983.
- [21] Z. Liu, Y. Yang, S. Liang, B. Lu, J. Zhou, *Small Struct.*, **2021**, 2, 2100119.
- [22] X. Li, Z. Xu, Y. Qian, Z. Hou, *Energy Storage Mater.*, **2022**, 53, 72.
- [23] X. Huang, X. Liu, H. Li, Q. Zhao, T. Ma, *Small Struct.*, **2022**, 4, 2200221.
- [24] H. Luo, B. Wang, J. Jian, F. Wu, L. Peng, D. Wang, *Mater. Today Energy*, **2021**, 21, 100799.
- [25] J. Zhu, M. Yang, Y. Hu, M. Yao, J. Chen, Z. Niu, *Adv. Mater.*, **2023**, 36, 2304426.
- [26] G. Ma, L. Miao, Y. Dong, W. Yuan, X. Nie, S. Di, Y. Wang, L. Wang, N. Zhang, *Energy Storage Mater.*, **2022**, 47, 203.
- [27] S. Zhang, H. Ao, J. Dong, D. Wang, C. Wang, X. Xu, Z. Hou, J. Yang, *Angew. Chem. Int. Ed.*, **2025**, 64, e202414702.
- [28] S. Li, Y. Zhong, J. Huang, G. Lai, L. Li, L. Jiang, X. Xu, B. Lu, Y. Liu, J. Zhou, *Energy Environ. Sci.*, **2025**, 18, 2599.
- [29] R. Guo, X. Liu, F. Xia, Y. Jiang, H. Zhang, M. Huang, C. Niu, J. Wu, Y. Zhao, X. Wang, C. Han, L. Mai, *Adv. Mater.*, **2022**, 34, 2202188
- [30] J. Dong, L. Su, H. Peng, D. Wang, H. Zong, G. Wang, J. Yang, *Angew. Chem. Int. Ed.*, **2024**, 63, e202401441.
- [31] S. Guo, L. Qin, J. Wu, Z. Liu, Y. Huang, Y. Xie, G. Fang, S. Liang, *Natl. Sci. Rev.*, **2024**, 11, nwae181.
- [32] J. Huang, Y. Zhong, H. Fu, Y. Zhao, S. Li, Y. Xie, H. Zhang, B. Lu, L. Chen, S. Liang, J. Zhou, *Adv. Mater.*, **2024**, 36, 2406257.
- [33] X. Hu, Z. Zhao, Y. Yang, H. Zhang, G. Lai, B. Lu, P. Zhou, L. Chen, J. Zhou, *InfoMat*. **2024**, 6, e12620.
- [34] F. Wang, J. Zhang, H. Lu, H. Zhu, Z. Chen, L. Wang, J. Yu, C. You, W. Li, J. Song, Z. Weng, C. Yang, Q. Yang, *Nat. Commun.*, **2023**, 14, 4211.
- [35] M. Li, X. Wang, J. Hu, J. Zhu, C. Niu, H. Zhang, C. Li, B. Wu, C. Han, L. Mai, *Angew. Chem. Int. Ed.* **2023**, 62, e202215552.